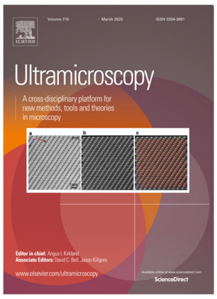

Characterisation of engineered defects in extreme ultraviolet mirror substrates using lab-scale extreme ultraviolet reflection ptychography

Haoyan Lu, Michal Odstrčil, Charles Pooley, Jan Biller,
Mikheil Mebonia, Guanze He, Matthew Praeger, Larissa Juschkin,
Jeremy Frey, William Brocklesby

PII: S0304-3991(23)00037-2
DOI: https://doi.org/10.1016/j.ultramic.2023.113720
Reference: ULTRAM 113720

To appear in: *Ultramicroscopy*

Received date : 5 December 2022
Revised date : 8 March 2023
Accepted date : 14 March 2023

Please cite this article as: H. Lu, M. Odstrčil, C. Pooley et al., Characterisation of engineered defects in extreme ultraviolet mirror substrates using lab-scale extreme ultraviolet reflection ptychography, *Ultramicroscopy* (2023), doi: https://doi.org/10.1016/j.ultramic.2023.113720.

Characterisation of engineered defects in extreme ultraviolet mirror substrates using lab-scale extreme ultraviolet reflection ptychography

HAOYAN LU,[1,2] MICHAL ODSTRČIL,[1,2,6] CHARLES POOLEY,[1] JAN BILLER,[2,3] MIKHEIL MEBONIA,[2,3] GUANZE HE,[4] MATTHEW PRAEGER,[1] LARISSA JUSCHKIN,[2,3] JEREMY FREY,[5] AND WILLIAM BROCKLESBY[1,*]

[1] *Zepler Institute, University of Southampton, Southampton SO17 1BJ, UK*
[2] *Experimental Physics of EUV, JARA-FIT, RWTH Aachen University, 52074 Aachen, Germany*
[3] *Peter Grünberg Institut (PGI-9), JARA-FIT, Forschungszentrum Jülich GmbH, 52425 Jülich, Germany*
[4] *Department of Engineering Science, University of Oxford, Oxford OX1 3PJ, UK*
[5] *Department of Chemistry, University of Southampton, Southampton SO17 1BJ, UK*
[6] *Currently with Carl Zeiss SMT, Carl-Zeiss-Straße 22, 73447 Oberkochen, Germany*
[*] *wsb@orc.soton.ac.uk*
https://zepler.soton.ac.uk/people/wsb

Abstract: Ptychography is a lensless imaging technique that is aberration-free and capable of imaging both the amplitude and the phase of radiation reflected or transmitted from an object using iterative algorithms. Working with extreme ultraviolet (EUV) light, ptychography can provide better resolution than conventional optical microscopy and deeper penetration than scanning electron microscope. As a compact lab-scale EUV light sources, high harmonic generation meets the high coherence requirement of ptychography and gives more flexibilities in both budget and experimental time compared to synchrotrons. The ability to measure phase makes reflection-mode ptychography a good choice for characterising both the surface topography and the internal structural changes in EUV multilayer mirrors. This paper describes the use of reflection-mode ptychography with a lab-scale high harmonic generation based EUV light source to perform quantitative measurement of the amplitude and phase reflection from EUV multilayer mirrors with engineered substrate defects. Using EUV light at 29.6 nm from a tabletop high harmonic generation light source, a lateral resolution down to ~ 88 nm and a phase resolution of 0.08 radians (equivalent to topographic height variation of 0.27 nm) are achieved. The effect of surface distortion and roughness on EUV reflectivity is compared to topographic properties of the mirror defects measured using both atomic force microscopy and scanning transmission electron microscopy. Modelling of reflection properties from multilayer mirrors is used to predict the potential of a combination of on-resonance, actinic ptychographic imaging at 13.5 nm and atomic force microscopy for characterising the changes in multilayered structures.

1. Introduction

Ptychography, sometimes also referred to as scanning coherent diffraction imaging (CDI), measures multiple scatter patterns from a coherently-illuminated sample and then uses algorithmic reconstruction to reconstruct an image of the sample containing quantitative phase and amplitude information, and also the complex illumination function of the probe light used to illuminate the sample. Ptychographic imaging is free from lens aberrations, and its resolution is limited by detector numerical aperture (NA), rather than by the size of the illuminating spot. Unlike typical microscope imaging system, the real-space image is not measured directly, but reconstructed from the diffraction patterns by iterative algorithms after applying constraints in both real and reciprocal spaces. Many different varieties of applications have been demonstrated successfully, at visible [1], EUV [2], soft X-ray [3], hard X-ray wavelengths [4], and using electrons [5, 6]. Ptychography is mostly used in a transmission-mode geometry, which limits the thickness of sample up to a few micrometers depending on the working wavelength. Reflection-mode ptychography is an emerging technique for characterising planar samples [7–9] and thin films [10]. Using the retrieved complex reflectivity of the sample surface, the surface 3D structures can also be reconstructed [10–12].

The capability of imaging surface features and the ability to measure phase make reflection-mode ptychography a good choice for characterising EUV multilayer mirrors. Multilayer mirrors are an important type of reflection optics widely used in the EUV regime. In EUV lithography (EUVL), they are used both as reflection optics and as the base structures of reflective masks. Defect detection and removal in these multilayered structures is one of the critical challenges for controlling illumination quality and mask printibility. In addition, knowledge of the phase changes upon reflection from the EUV masks is critical in predicting the aerial image on wafers because the phase plays an important role in the 3D mask effects, like shadowing, telecentricity errors and best-focus shifts [13, 14]. Some inspection methodologies have already been demonstrated successfully, but rarely have the capability to provide phase information. For example, *actinic* inspection methodologies which use light at the same wavelength as the designed working wavelength, like bright field [15, 16] and dark field [17, 18] EUV microscopy, have the ability to scan large surfaces for the presence of small printable defects. Non-optical inspection techniques, such as scanning electron microscopy (SEM) [19] and atomic force microscopy (AFM) [20], can be used for topographic measurements with varying spatial resolutions. However, they are typically not able to provide information about phase errors in the reflected wavefront. EUV ptychographic imaging provides better resolution than visible light microscopy and deeper penetration than SEM and AFM. Reflection-mode ptychography, which provides complex reflectivity information, has potential applications in verifying the design of phase shift masks and helps simulating their aerial image [21, 22]. Most of the research so far has been demonstrated on synchrotron light sources [23–26] because of the source's strengths in photon flux, coherence and stability. However, the large investment, huge facility size and limited experimental time impede further applications. High-harmonic generation (HHG) is a promising alternative EUV light source, given its small footprint, high coherence and acceptable photon flux. Many demonstrations of EUV ptychography using HHG-based light sources have been reported in the fields of tomography [27], characterisation of material components [10, 11, 28], wavefront sensing [29] and coherent imaging [30–33]. Relevant to the topic of this paper, HHG-based ptychographic inspections of defects in EUV masks have been demonstrated on patterned masks [24, 34].

In this paper, we describe the use of reflection-mode ptychography with a HHG-based light source for imaging of the complex EUV reflectivity of a silicon/molybdenum based multilayer mirror structure grown on a substrate containing prefabricated defects in the shape of etched pits. The EUV reflectivity at a wavelength of 29.6 nm is compared to the physical properties of the mirror measured using AFM and scanning transmission electron microscopy (STEM). AFM can help decouple the phase contributions from structural changes and topographic changes. Due to the shallow penetration depth at 29.6 nm, away from the mirror's designed wavelength, the phase shifts introduced by the changes in multilayered structure are small. The topography derived from phase is shown to agree well with AFM measurements. Shadowing of walls on both sides of the pit defects due to the 45° incident angle is accurately reproduced in the images. Given the recorded phase and amplitude noise levels in the complex reflectivity, modelling of reflection properties from multilayer mirrors is used to predict the capability of a combination of ptychography and AFM to study internal changes in the multilayered structure at both 29.6 nm and 13.5 nm.

2. Experimental setup

The HHG system uses 45 fs ultrafast laser pulses at 800 nm, with energies of ~ 1.4 mJ at a repetition rate of 1 kHz. These pulses are focused onto a gas cell filled with 80 mbar argon gas. The beam has a diameter of FWHM ≈ 70 µm at the focus, giving a peak intensity ~ 10^{15} W/cm^2. The residual infrared light is blocked by a 200 nm thick aluminium filter while the EUV light at the 27th harmonic of the laser (29.6 nm/42 eV) is attenuated by ~ 40%. Harmonics are further filtered by a single spherical narrow-band multilayer mirror. After filtering, the spectrum illuminating the sample consists of three harmonics centred around 29 nm while the central 27th harmonic contains more than 80% of the total power. The resulting flux is ~ 10^8 photons/s [30]. The EUV beam is focused down to FWHM ≈ 15 µm on the aperture panel which is held 50 µm ~ 150 µm above the sample surface. As illustrated in fig. 1 (a), the reflected light is collected by a XUV CCD camera (Andor DX434) whose surface is perpendicular to the specular reflection.

2.1. Sample design and fabrication

The sample is a Si/Mo multilayer mirror structure with pre-designed defects in the form of pits etched into the Si substrate before the multilayer is deposited, to simulate phase defects. The defect patterns have the shape of an adapted 1951 USAF resolution test chart. The pattern consists of bars in groups of three with different sizes; their lengths range from 2.0 µm to 28.4 µm and their depths are measured to be ~ 367 nm by white light interferometer. Multiple copies of the patterns are etched into the silicon substrate by e-beam lithography before deposition of 144 periods of Si/Mo (4.14 nm /2.76 nm) in a multilayered structure. The fabrication was done by optiX fab GmbH. This sample is designed to have peak reflectivity at λ = 13.5 nm at an angle of incidence of 6°, the same working condition as masks used in high-volume manufacturing.

2.2. Ptychography geometry

In a reflection geometry, radiation is incident on a flat sample, which defines the X-Y plane, at an angle to the surface normal, the Z axis (all quoted angles are relative to the surface normal). As a lab-based EUV light source, the available coherent EUV photon flux from a HHG light source is rather limited. It is optimal to work at an incident angle with a reflectivity as high as possible to maximise both signal/noise and NA-limited resolution. Fig. 1(b) shows the variation of Abbé resolution (red) and sample reflectivity (blue) as a function of angle of incidence for 29.6 nm light. The lateral resolution r in the direction parallel to the incident plane will be worse than in the orthogonal direction because its collected spatial frequency range is smaller, which is caused by the tilted imaging geometry [35]. At 29.6 nm, an incident angle of 45° allows a high NA (~0.39 perpendicular to the plane of incidence) and a reflectivity of ~ 4.5%, which is a good compromise for resolution and signal/noise. The theoretical resolution limit in this case is $r_\perp \approx 37$ nm and $r_\parallel \approx 52$ nm.

2.3. Design of aperture panel

Ptychography is most effective when the shape of the illuminating beam on the sample contains sufficient amount of structures [36, 37], rather than the low spatial frequencies found in, for example, a Gaussian-shaped beam. The illumination probe is formed by focusing the beam through a structured aperture placed close enough to the sample, which will avoid coherent flux losses caused by other probe forming methods such as Fresnel zone plate. In transmission this is easily achieved; in reflection, this adds considerable complexity to the geometry, as the reflected beam needs to pass near the aperture used for illumination, as illustrated in fig. 1 (c). The aperture panel is designed to have two windows, for the incident and reflected beams respectively. The windows are fabricated by ultrafast laser drilling through a 3 µm thick copper foil. The aperture is designed to be installed at a distance of ~ 100 µm in front of the sample. A similar

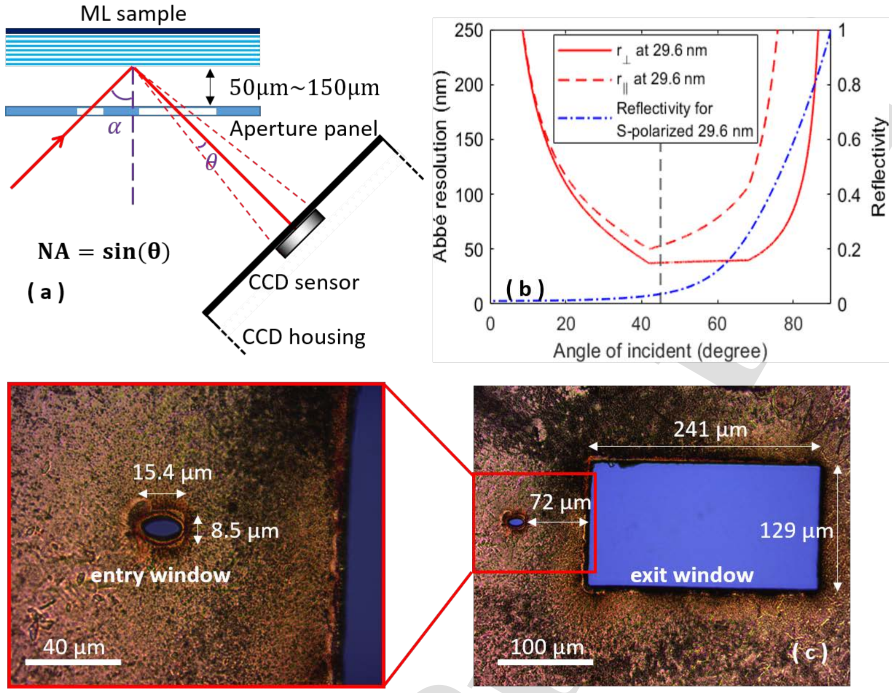

Fig. 1. (a) is a schematic showing the setup geometry. The sizes of items are not to scale. (b) plots the theoretical Abbé resolution and reflectivity from the multilayered (ML) sample at different angles of incidence α, showing the best resolution happening near 45°. (c) shows microscopic images of double windows on the aperture panel before they are deposited with soot.

double window design was also used in [38] but only for low NA imaging when the incident angle is close to normal.

2.4. *Parasitic reflection mitigation*

Since the two windows are very close together, any reflected light from around the entry window will form background noise, reducing signal-to-noise ratio greatly, especially if the focused beam is not well aligned. A thin layer of soot, whose particles have diameters of 30 nm~50 nm [39], was deposited on the aperture panel to reduce the parasitic reflection. Comparing the reflection intensity from a Au coated Si substrate before and after soot deposition, a reflectivity decrease of at least 3 orders of magnitude was measured. Fig. 2 shows the reconstructed probe when the aperture panel was used in a conventional transmission-mode setup; (a) is the probe at object plane while (b) is at the aperture plane after propagating back using the angular spectrum method (ASM). The clusters of soot particles around the aperture edges produce an appropriately-structured probe beam which helps the convergence and stability of the ptychographic iterative optimisation [37].

3. Data collection and processing

The translations of aperture and sample are separately controlled by two 3-axis piezoelectric stages. The probe at the sample plane is slightly bigger than the entry window, which is about 15 µm × 9 µm. A scan step of 4 µm renders a linear overlap between neighbouring scans more than 60%, which meets the requirement of 60% overlap recommended in [40]. Our measurement

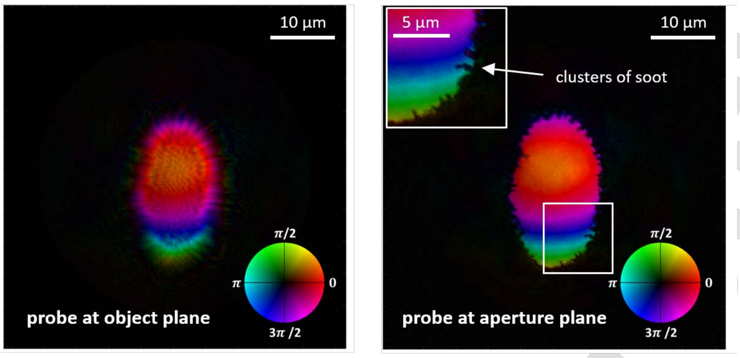

(a) (b)

Fig. 2. (a) and (b) show the reconstructed probe electric field at object plane and aperture plane respectively, plotted with hue, saturation and value (HSV) colour wheel, with phase and modulus being represented by hue and value respectively. The probe at the aperture plane is generated by propagating the reconstructed probe at the sample back by the aperture-sample spacing using ASM. Clusters of soot particles can be seen around the aperture edges.

consists of 117 scans in the X-Y plane following a Fermat spiral scan path [41] and covers an area of 40 µm × 40 µm. The CCD is positioned ∼ 27 mm downstream of the sample. Without any data cropping, the 1024 pixels × 1024 pixels (13 µm × 13 µm per pixel) sensor provides a collection NA of 0.24. The theoretical upper value at this angle, NA = 0.39, was not used in order to avoid any accidental contact between the CCD and the sample holder. The dynamic range of the diffraction signal is increased by the use of multiple CCD exposures with different exposures times, which are combined to make a single frame. The maximum exposure is 40 s while the minimum is selected dynamically to avoid possible signal saturation. The total acquisition time is about 3 hours, giving about 90 s for each scan position. The time overhead of data reading is more than 50% because of the use of a slow CCD readout rate (31kHz) to minimise readout noise.

Ptychographic reconstruction was performed with the PtychoShelves software suite [42]. All diffraction patterns are first corrected with the tilted plane correction (TPC) method proposed in [7] before fed into the iterative reconstruction. The ptychographic reconstruction is done with an initial 300 iterations of a difference map (DM) algorithm [43], followed by 2000 iterations of a least-squares maximum-likelihood (LSQ-ML) algorithm [44]. Partial coherence is accounted for by reconstructing 4 incoherent states for the probe using the state mixtures method by Thibault & Menzel [45]. Additionally, with the orthogonal probe relaxation (OPRP) method [46], 4 orthogonal modes of probe were used for the dominant probe state to consider the EUV output intensity and probe wavefront fluctuations.

4. Results

In order to observe the cross section of multilayered structures, a ∼ 15 µm × 5 µm lamella, crossing the three-bar features almost perpendicularly, was cut by focused ion beam (FIB). Fig. 3 shows the side view of the lamella measured by STEM. The substrate pits are clearly visible, and the distortion of the multilayers grown over the pitted substrate can be seen. All these STEM images are collected in high-angle annular dark field (HAADF) mode, where high-Z elements like Mo generate stronger signals than low-Z elements like Si and C (protective coating for FIB cutting). Thus the alternate dark and bright lines seen, for example, in (b) represent the layered

Si and Mo structures respectively.

The topography of the Si substrate has a significant effect on the periodicity of the deposited Si/Mo layers. For example, for an area with a small bump on the substrate (blue rectangle in fig. 3) or an area with a sloping side wall (red rectangle), the regularity of layered structures above will be disturbed, even being folded. But these defects can be concealed if sufficient number of layers are deposited. Surface inspection tools, like AFM and SEM, will not be able to detect the defects in this case. On the contrary, actinic inspection like reflection-mode EUV ptychography is still capable of detecting hidden defects because of the penetration depth of EUV light into the multilayered structures. Calculations using the IMD package [47] within XOP [48] show that EUV light at resonance can penetrate ~ 50 nm into the multilayered structures, and close to resonance the penetration depth can be up to 200 nm.

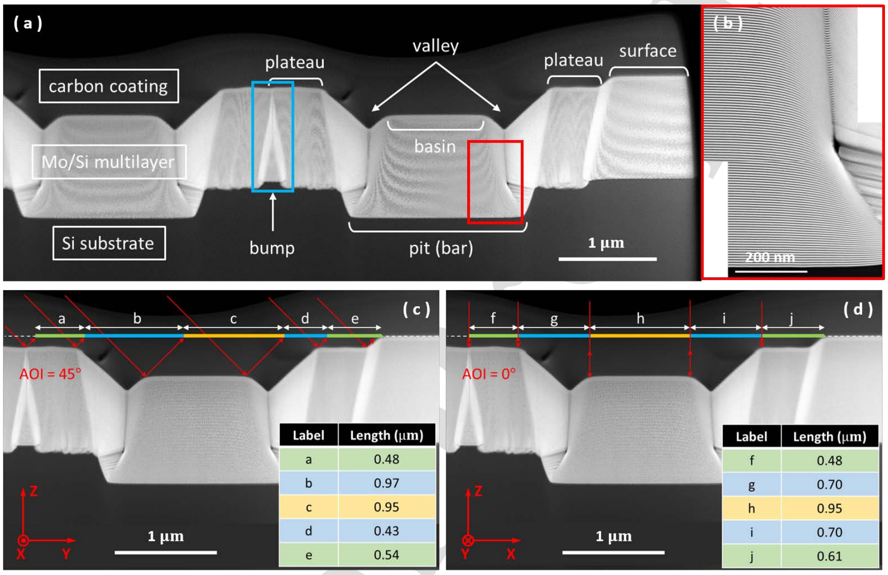

Label	Length (µm)
a	0.48
b	0.97
c	0.95
d	0.43
e	0.54

Label	Length (µm)
f	0.48
g	0.70
h	0.95
i	0.70
j	0.61

Fig. 3. (a) is the STEM-HAADF image of the cross section of the multilayered structures above the pit features in the substrate. Different regions are named for reference based on their topographic resemblance. The areas within the blue and red rectangles have a bump and a slope feature on the substrate respectively. (b) shows the zoomed-in image for the structures near the slope. The layered structures are squeezed during deposition to be folded. (c) and (d) illustrate the situations when the incident plane is perpendicular to or parallel to the long axis of the bar-shaped substrate patterns respectively. The widths of each region with different reflectivities are measured and listed in the images.

4.1. Reflectivity analysis

Ptychography measures the full complex reflectivity of the sample, unlike incoherent microscopy techniques. The square modulus of the complex reflected electric field is proportional to the reflectivity of the sample, even though the absolute value can not be retrieved unless the probe intensity is known and stable, as shown in [11]. The variation of the reflectivity over the whole scan area is influenced by many factors, including surface roughness, structural regularity and angle of incidence. Based on the structure's profile shown in fig. 3, only two areas are capable of providing high reflectivity: the bottom of the basin and the top surface, which are both smooth and regular structures. The plateau regions have low reflectivity because the reactive ion etching during the pattern formation after e-beam lithography introduces undesired roughness on the substrate.

Fig. 4 (a) shows the reflected electric field amplitude when the plane of incidence of the EUV light is the Y-Z plane. The EUV is incident at an angle of 45° to the surface normal. The variation in reflected amplitude arises from changes in angle of incidence and from surface roughness, with both factors contributing to the low-reflectivity areas around each feature. Fig. 4 (b) and (c) plot the modulus variation across the three-bar features in either the Y-Z (b) or X-Z (c) plane. In order to increase the signal-to-noise ratio in analysis, modulus values are averaged along the bar orientation inside a selected rectangular area (shown in (a)). Since we only focus on relative values, all modulus values are normalised by the average value at the surface. The plateaus have an averaged modulus value of ~ 0.44, showing that their reflectivity is decreased to only about 1/5 of the normal value because of the substrate roughness in this area. The widths of each region can be verified by reference to the STEM cross-sections in fig. 3 (c) and (d), which illustrate two situations when the incident plane is perpendicular to and along the bar features. Yellow, blue and green lines represent basin, valley and plateau regions respectively.

Fig. 4 (b) shows that the basin region reflections are offset when the plane of incidence is perpendicular to the long axis of the bars. The left valley region is 0.52 µm wider than the right. The offset arises from the depth of the basins, which at 45° causes the reflection to be shifted compared to a reflection from the surface, and indicates the fidelity of the reconstruction process, including the correction of the diffraction patterns for tilt.

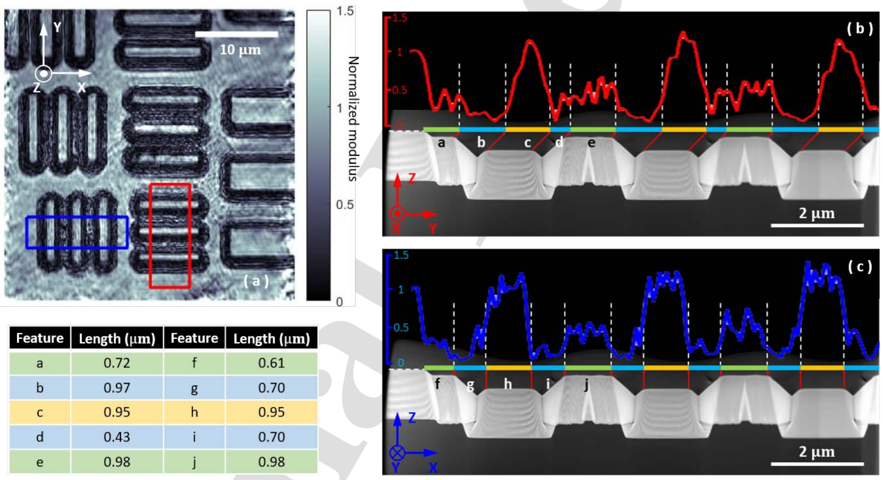

Feature	Length (µm)	Feature	Length (µm)
a	0.72	f	0.61
b	0.97	g	0.70
c	0.95	h	0.95
d	0.43	i	0.70
e	0.98	j	0.98

Fig. 4. (a) Amplitude of the sample reflectivity, normalised to the averaged value on the top surface. The EUV light is incident in the Y-Z plane. (b), (c) Average amplitude reflectivity within the regions marked with red and blue rectangles. The STEM-HAADF images of the sample are shown below each graph for reference. In (b) the plane of incidence lies across the long axis of the bars, so that the high-reflectivity basin regions appear shifted laterally because of their depth. In (c), the plane of incidence is along the long axis of the bars, so that no lateral shifts of the basin regions are seen.

4.2. Phase analysis

For multilayered structures, the phase of the reflected light is more sensitive to the periodicity change and topography than the amplitude, and ptychography provides a direct measurement of the phase of the reflected light without the use of interferometry.

Fig. 5 (a) illustrates the complex electric field reflected from elements 1 and 2 in group 7 of the USAF test pattern, where the field modulus and phase are represented using a HSV colour wheel.

Fig. 5 (d) shows one of the corrected diffraction patterns used to reconstruct (a). The plane of incident on the object is the Y-Z plane. The phase shifts due to the changes in depths and in the mirror layered structures are seen clearly as colour variations between the surface and the basin regions inside each element. The border area around each element is noisy, because in these regions the reflectivity is very low and the phase is changing rapidly along the sloping sides of the pits. An averaged phase of the regions highlighted by white rectangles is shown in fig. 5 (b) and (c). Phase steps are seen between the surface level shown at the edges of the figures (blue), and the regions corresponding to the basin (red). The measured phase shifts between surface and bottom of the basin are 2.02 radians and 1.83 radians for two cases respectively. In addition, distinct phase curvature is observed inside the basin regions, where the observed 'humps' in phase have an magnitude of 1.00 radians and 0.89 radians respectively.

Two separate effects may contribute to the phase of light reflected from a multilayer mirror with structures like the ones used here: path differences due to surface topography, and changes in the multilayered structure itself due to subsurface defects. These two intertwined effects are difficult to decouple by using only one technique.

In the first case, the steps in the surface will create path differences for the reflected light, which will translate into phase differences in the measured image. The phase difference $\Delta\phi$ between the reflected wavefronts from basin and surface regions will follow the equation:

$$\Delta\phi = (2d\cos\alpha - m\lambda)\cdot 2\pi/\lambda \tag{1}$$

where d is the depth of basin relative to the surface, α is the incident angle relative to normal and m is the number of full cycles when the phase is wrapped. The m value can be determined by finding the closest phase-derived-depth to an AFM or white light interferometry measurement. An alternative method is to do two or more measurements with either different wavelengths or different angles of incidence.

The second contribution to the measured phase of the reflected light arises from the underlying multilayer structure. The phase of light reflected by a multilayer mirror changes strongly depending on the resonance between input wavelength and the multilayer period, undergoing a π phase shift from one side of the resonance to the other. Thus for a given wavelength, any changes in the multilayered structure, such as variation in the layer period, can cause large changes in the phase of reflected light, particularly around the wavelength of peak reflectivity. The STEM image in fig. 3 shows that, changes in multilayer period do occur in the samples used in this experiment in areas where there are sub-surface defects. To give an idea of the scale of the possible phase changes of the reflected light arising from multilayer changes, at ~13.5 nm and $\alpha = 6°$, the peak reflection wavelength of the mirror in this experiment, the phase shift of the reflected light for a 1% change in multilayer period is calculated to be 0.47 radians. The same multilayer period change at 29.6 nm and $\alpha = 45°$ results in only 0.006 radians phase shift, because the wavelength is a long way from the multilayer resonance.

Comparing the two different variation mechanisms, it is clear that at the wavelength used in this experiment the dominant phase shift will be caused by changes in depth of the surfaces from which the EUV is reflected. Inside the basin regions, a phase 'hump' can be interpreted as a topographic dent. As shown in fig. 5 (e)(f), the phase-derived-profile calculated by equation 1 agrees well with the AFM measurements, which proves that the measured phase shift arises principally from the topographic change, rather than any changes in the multilayered structures.

The lateral resolution in the final reconstruction is quantified by the knife-edge method exploiting the fact that the boundaries of basin regions are known to have sharp edges. Two regions in fig. 5 (a), marked by blue rectangles, are chosen to calculate the resolution in two directions. The modulus profile is averaged along the bar feature direction and then fitted by the complementary error function (ERFC). If 10%-90% is set as the criterion, horizontal and vertical resolutions are 88 nm and 154 nm respectively. The difference between two directions

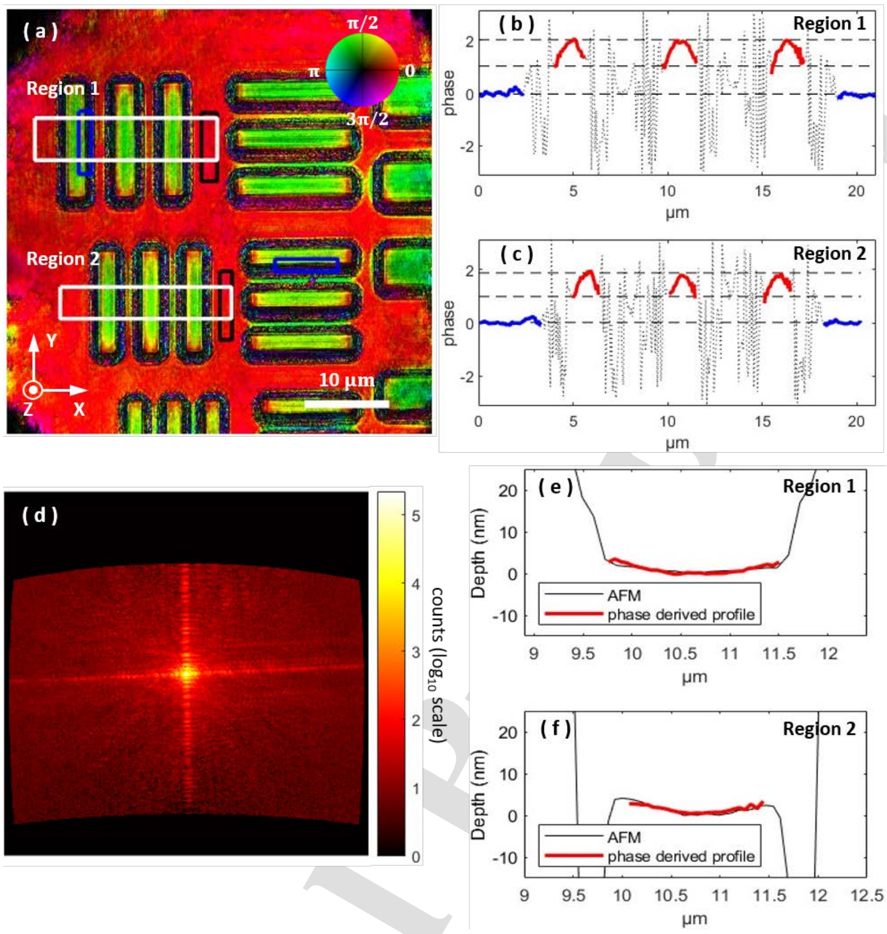

Fig. 5. (a) Complex reflectivity of multilayer sample, where colour indicates phase and intensity indicates amplitude (see inset colour wheel). Changes in phase due to the depth profile are clearly seen, as is bending of the basin regions around the edges where deposition has been distorted. Two blue rectangles mark the regions for calculating the resolution with knife-edge method. Two black rectangles mark the regions for calculating the standard deviation of the reconstructed phase (b), (c) Phase of the reflected signal, averaged over the white boxes indicated as Region 1 and Region 2 in (a). The surface and basin regions are indicated by blue and red lines respectively, and the sidewall regions indicated by black dotted lines. (d) plots one of the diffraction patterns after TPC correction, which will cause the loss of high frequency signals. (e), (f) AFM measurements are plotted with black lines, while phase-derived-profile of basin regions are plotted with red lines in the same scale. The topographic bending of basin regions agrees well between two measurements.

are mainly attributed to the loss of high-frequency signals caused by tilted geometry.

4.3. Phase noise and multilayered structure defects

In order to assess the capability of the technique to measure variations in the multilayered structure, both in this geometry and in actinic near-normal incidence geometry, a statistical measure of the noise in the reconstructed images is required.

Over areas of the sample which are expected to be free of defects or topographic changes (black rectangles in fig. 5 (a)), the standard deviation of the phase measured is 0.08 radians, and the standard deviation of the amplitude reflection is 9.3%. In the experimental geometry used here, with $\lambda = 29.6$ nm and an incident angle of 45°, the measured phase noise is equivalent to a height variation at the sample of 0.27 nm, which is equivalent to the change in phase generated by a 20% variation in multilayer period. The relative insensitivity of the phase to mirror period changes at $\lambda = 29.6$ nm arises from the fact that the wavelength is off-resonance with the mirror's design wavelength.

4.4. Application to 13.5 nm imaging

On-resonance inspection of defects in multilayered structures is of great interest because of a deeper penetration, a higher reflectivity and a higher sensitivity of reflected phase to structural changes. As for mirrors and masks used in EUVL, an actinic ptychographic inspection at 13.5 nm will reveal the complex wavefront when installed in the industrial environments. EUV ptychography with a 13.5 nm HHG-based light source has already shown applications in imaging or inspecting patterned EUV masks [24, 34, 49], characterising element components [28] and evaluating EUV pellicle properties [50]. However, HHG will generally have smaller photon flux at higher energy because of its lower conversion efficiency. While imaging at 13.5 nm is not performed in this study because of experimental constraints, the capability of HHG-based ptychography to measure phase defects can be predicted based on the measured noise performance of the present experiments.

Assuming the same RMS phase noise (0.08 radians) as measured in these experiments, if imaging using an incident wavelength of 13.5 nm and an incident angle of 6°, the designed working condition, the observable change in the multilayer period would be 0.17%. This high sensitivity stems from the narrow resonance of the mirror reflectivity. In contrast, the change in amplitude reflectivity for the same multilayer period change is much smaller, only 0.7%, because the amplitude change at the peak of the resonance is much smaller than the phase change.

In order to separate phase changes due to surface topography from those due to mirror multilayer period, it is necessary to compare the measurements of phase with surface profile measurements from AFM. As is shown here, correlation of the two measurements on a single sample is straightforward. Thus on-resonance, 13.5 nm ptychographic imaging with the same noise floor as observed at 29.6 nm would be an extremely sensitive probe of the kind of sub-surface layer thickness variation seen in the STEM images of defect samples.

5. Conclusion

Reflection-mode ptychography using a tabletop EUV light source based on HHG has been used, together with STEM and AFM, to characterise the changes in reflectivity of an EUV mirror with engineered substrate defects. Ptychography allows measurement of both phase and amplitude of the reflected light, with a lateral resolution down to 88 nm. The use of an incident angle of 45° allows a relatively large numerical aperture (NA $\approx$ 0.24) for the detector, improving resolution, but highlights the shadowing effect produced by the steps in the surface profile.

Both the amplitude and the phase images of the mirror sample agree well with AFM and STEM measurements. Reduction of reflectivity amplitude due to surface roughness is observed in areas identified as rough on the STEM images, and changes in the phase of the reflected light agree well with height measurements from AFM, with a baseline noise level equivalent to 0.27 nm RMS height variation. The origin of the insensitivity of phase variation to mirror multilayered structure variation is shown via modelling of the mirror reflectivity.

Modelling of mirror reflectivity further indicates that similar experiments performed at 13.5 nm, in resonance with the mirror reflection peak, would be able to identify variations in the mirror period of less than 0.2% as a function of position across the sample surface. The combination of topography measurement by AFM or white light interferometry with EUV ptychography, potentially at multiple wavelengths, would be a powerful combination for measurement of both surface height variation and sub-surface mirror structure changes for full characterisation of laterally-structured EUV multilayers, such as EUV phase shift masks.

6. Backmatter

Funding. This work builds on the investment and research from the EPSRC Basic Technology grant GR/R87307/01. H.L. acknowledges Erasmus Mundus Joint Doctorate Programme EXTATIC scholarship from EACEA grant 2012-0033.

Acknowledgements. L.J. acknowledges financial support from the Helmholtz Association for a Helmholtz professorship as part of the Initiative and Network Fund. C.P. acknowledges the EPSRC scholarship.

Disclosures. The authors declare that there are no conflicts of interest related to this article.

Data Availability. Data underlying the results presented in this paper are available in PURE, the University of Southampton's research information system.

References

1. J. Rodenburg, A. Hurst, and A. Cullis, "Transmission microscopy without lenses for objects of unlimited size," Ultramicroscopy **107**, 227–231 (2007).
2. P. D. Baksh, M. Ostrčil, M. Miszczak, C. Pooley, R. T. Chapman, A. S. Wyatt, E. Springate, J. E. Chad, K. Deinhardt, J. G. Frey, and W. S. Brocklesby, "Quantitative and correlative extreme ultraviolet coherent imaging of mouse hippocampal neurons at high resolution," Sci. Adv. **6**, eaaz3025 (2020).
3. D. A. Shapiro, S. Babin, R. S. Celestre, W. Chao, R. P. Conley, P. Denes, B. Enders, P. Enfedaque, S. James, J. M. Joseph, H. Krishnan, S. Marchesini, K. Muriki, K. Nowrouzi, S. R. Oh, H. Padmore, T. Warwick, L. Yang, V. V. Yashchuk, Y. S. Yu, and J. Zhao, "An ultrahigh-resolution soft x-ray microscope for quantitative analysis of chemically heterogeneous nanomaterials," Sci. Adv. **6** (2020).
4. J. M. Rodenburg, A. C. Hurst, A. G. Cullis, B. R. Dobson, F. Pfeiffer, O. Bunk, C. David, K. Jefimovs, and I. Johnson, "Hard-X-Ray Lensless Imaging of Extended Objects," Phys. Rev. Lett. **98**, 034801 (2007).
5. P. D. Nellist, B. C. McCallum, and J. M. Rodenburg, "Resolution beyond the 'information limit' in transmission electron microscopy," Nature **374**, 630–632 (1995).
6. Z. Chen, Y. Jiang, Y.-T. Shao, M. E. Holtz, M. Odstrčil, M. Guizar-Sicairos, I. Hanke, S. Ganschow, D. G. Schlom, and D. A. Muller, "Electron ptychography achieves atomic-resolution limits set by lattice vibrations," Science **372**, 826–831 (2021).
7. D. F. Gardner, B. Zhang, M. D. Seaberg, L. S. Martin, D. E. Adams, F. Salmassi, E. Gullikson, H. Kapteyn, and M. Murnane, "High numerical aperture reflection mode coherent diffraction microscopy using off-axis apertured illumination," Opt. Express **20**, 19050 (2012).
8. M. Zürch, C. Kern, and C. Spielmann, "XUV coherent diffraction imaging in reflection geometry with low numerical aperture," Opt. Express **21**, 21131 (2013).
9. C. L. Porter, M. Tanksalvala, M. Gerrity, G. Miley, X. Zhang, C. Bevis, E. Shanblatt, R. Karl, M. M. Murnane, D. E. Adams, and H. C. Kapteyn, "General-purpose, wide field-of-view reflection imaging with a tabletop 13 nm light source," Optica **4**, 1552 (2017).
10. M. Tanksalvala, C. L. Porter, Y. Esashi, B. Wang, N. W. Jenkins, Z. Zhang, G. P. Miley, J. L. Knobloch, B. McBennett, N. Horiguchi, S. Yazdi, J. Zhou, M. N. Jacobs, C. S. Bevis, R. M. Karl, P. Johnsen, D. Ren, L. Waller, D. E. Adams, S. L. Cousin, C.-T. Liao, J. Miao, M. Gerrity, H. C. Kapteyn, and M. M. Murnane, "Nondestructive, high-resolution, chemically specific 3D nanostructure characterization using phase-sensitive EUV imaging reflectometry," Sci. Adv. **7**, eabd9667 (2021).
11. E. R. Shanblatt, C. L. Porter, D. F. Gardner, G. F. Mancini, R. M. Karl, M. D. Tanksalvala, C. S. Bevis, V. H. Vartanian, H. C. Kapteyn, D. E. Adams, and M. M. Murnane, "Quantitative Chemically Specific Coherent Diffractive Imaging of Reactions at Buried Interfaces with Few Nanometer Precision," Nano Lett. **16**, 5444–5450 (2016).
12. M. D. Seaberg, B. Zhang, D. F. Gardner, E. R. Shanblatt, M. M. Murnane, H. C. Kapteyn, and D. E. Adams, "Tabletop nanometer extreme ultraviolet imaging in an extended reflection mode using coherent Fresnel ptychography," Optica **1**, 39 (2014).
13. A. Erdmann, D. Xu, P. Evanschitzky, V. Philipsen, V. Luong, and E. Hendrickx, "Characterization and mitigation of 3D mask effects in extreme ultraviolet lithography," Adv. Opt. Technol. **6**, 187–201 (2017).
14. A. Erdmann, P. Evanschitzky, H. Mesilhy, V. Philipsen, E. Hendrickx, and M. Bauer, "Attenuated phase shift mask for extreme ultraviolet: can they mitigate three-dimensional mask effects?" J. Micro/Nanolithography, MEMS, MOEMS **18**, 1 (2018).

15. L. Juschkin and R. Freiberger, “Two magnification steps EUV microscopy with a Schwarzschild objective and an adapted zone plate lens,” in *EUV and X-Ray Optics: Synergy between Laboratory and Space,* vol. 7360 R. Hudec and L. Pina, eds. (SPIE, 2009), p. 736005.
16. K. A. Goldberg, M. P. Benk, A. Wojdyla, I. Mochi, S. B. Rekawa, A. P. Allezy, M. R. Dickinson, C. W. Cork, W. Chao, D. J. Zehm, J. B. Macdougall, P. P. Naulleau, and A. Rudack, “Actinic mask imaging: recent results and future directions from the SHARP EUV microscope,” in *Extreme Ultraviolet (EUV) Lithography V,* vol. 9048 O. R. Wood and E. M. Panning, eds. (SPIE, 2014), p. 90480Y.
17. L. Juschkin, R. Freiberger, and K. Bergmann, “EUV microscopy for defect inspection by dark-field mapping and zone plate zooming,” J. Physics: Conf. Ser. **186**, 012030 (2009).
18. T. Suzuki, H. Miyai, K. Takehisa, H. Kusunose, H. Watanabe, and I. Mori, “Detection capability of Actinic Blank Inspection tool,” in *Photomask Japan 2015: Photomask and Next-Generation Lithography Mask Technology XXII,* N. Yoshioka, ed. (SPIE, 2015), p. 96580O.
19. W. Cho, V. L. Tolani, M. Satake, D. Price, P. A. Morgan, and D. Rost, “Classification and printability of EUV mask defects from SEM images,” in *International Conference on Extreme Ultraviolet Lithography 2017,* vol. 1045006 P. A. Gargini, K. G. Ronse, P. P. Naulleau, and T. Itani, eds. (SPIE, 2017), p. 5.
20. A. Zandiatashbar, B. Kim, Y.-k. Yoo, K. Lee, A. Jo, J. S. Lee, S.-J. Cho, and S.-i. Park, “Automatic defect review for EUV photomask reticles by atomic force microscope,” in *Photomask Technology 2015,* vol. 9635 N. Hayashi and B. S. Kasprowicz, eds. (2015), p. 96351A.
21. C. Constancias, M. Richard, D. Joyeux, J. Chiaroni, R. Blanc, J. Y. Robic, E. Quesnel, and V. Muffato, “Phase-shift mask for EUV lithography,” in *Emerging Lithographic Technologies X,* vol. 6151 M. J. Lercel, ed. (2006), p. 61511W.
22. A. Erdmann, P. Evanschitzky, H. Mesilhy, V. Philipsen, E. Hendrickx, and M. Bauer, “Attenuated phase shift mask for extreme ultraviolet: can they mitigate three-dimensional mask effects?” J. Micro/Nanolithography, MEMS, MOEMS **18**, 1 (2018).
23. T. Harada, H. Hashimoto, T. Amano, H. Kinoshita, and T. Watanabe, “Phase imaging results of phase defect using micro coherent EUV scatterometry microscope,” in *Photomask Technology 2015,* N. Hayashi and B. S. Kasprowicz, eds. (2015), p. 96351E.
24. Y. Nagata, T. Harada, T. Watanabe, H. Kinoshita, and K. Midorikawa, “At wavelength coherent scatterometry microscope using high-order harmonics for EUV mask inspection,” Int. J. Extrem. Manuf. **1**, 032001 (2019).
25. S. Fernandez, D. Kazazis, R. Rajendran, I. Mochi, P. Helfenstein, S. Yoshitake, and Y. Ekinci, “Comparative study of extreme ultraviolet absorber materials using lensless actinic imaging,” J. Micro/Nanolithography, MEMS, MOEMS **18**, 1 (2019).
26. I. Mochi, P. Helfenstein, I. Mohacsi, R. Rajeev, D. Kazazis, S. Yoshitake, and Y. Ekinci, “RESCAN: an actinic lensless microscope for defect inspection of EUV reticles,” J. Micro/Nanolithography, MEMS, MOEMS **16**, 041003 (2017).
27. M. Du, L. Loetgering, K. S. E. Eikema, and S. Witte, “Ptychographic optical coherence tomography,” Opt. Lett. **46**, 1337 (2021).
28. W. Eschen, L. Loetgering, V. Schuster, R. Klas, A. Kirsche, L. Berthold, M. Steinert, T. Pertsch, H. Gross, M. Krause, J. Limpert, and J. Rothhardt, “Material-specific high-resolution table-top extreme ultraviolet microscopy,” Light. Sci. & Appl. **11**, 117 (2022).
29. M. Du, X. Liu, X. Liu, A. Pelekanidis, A. Pelekanidis, F. Zhang, F. Zhang, L. Loetgering, P. E. Konold, C. L. Porter, P. Smorenburg, K. S. Eikema, K. S. Eikema, S. Witte, and S. Witte, “High-resolution wavefront sensing of multi-spectral high-harmonic generation sources using ptychography,” Imaging Appl. Opt. Congr. 2022 (3D, AOA, COSI, ISA, pcAOP) (2022), paper CF1D.2 p. CF1D.2 (2022).
30. P. Baksh, M. Odstrcil, A. Parsons, J. Bailey, K. Deinhardt, J. E. Chad, W. S. Brocklesby, and J. G. Frey, “Quantitative Evaluation of Hard X-ray Damage to Biological Samples using EUV Ptychography,” J. Physics: Conf. Ser. **849**, 012034 (2017).
31. L. Loetgering, S. Witte, and J. Rothhardt, “Advances in laboratory-scale ptychography using high harmonic sources [Invited],” Opt. Express **30**, 4133 (2022).
32. G. K. Tadesse, W. Eschen, R. Klas, M. Tschernajew, F. Tuitje, M. Steinert, M. Zilk, V. Schuster, M. Zürch, T. Pertsch, C. Spielmann, J. Limpert, and J. Rothhardt, “Wavelength-scale ptychographic coherent diffractive imaging using a high-order harmonic source,” Sci. Reports **9**, 1735 (2019).
33. N. X. Truong, R. Safaei, V. Cardin, S. M. Lewis, X. L. Zhong, F. Légaré, and M. A. Denecke, “Coherent Tabletop EUV Ptychography of Nanopatterns,” Sci. Reports **8**, 16693 (2018).
34. D. Mamezaki, T. Harada, Y. Nagata, and T. Watanabe, “Imaging performance improvement of coherent extreme-ultraviolet scatterometry microscope with high-harmonic-generation extreme-ultraviolet source,” Jpn. J. Appl. Phys. **56**, 06GB01 (2017).
35. B. Zhang, D. F. Gardner, M. D. Seaberg, E. R. Shanblatt, H. C. Kapteyn, M. M. Murnane, and D. E. Adams, “High contrast 3D imaging of surfaces near the wavelength limit using tabletop EUV ptychography,” Ultramicroscopy **158**, 98–104 (2015).
36. M. Guizar-Sicairos, M. Holler, A. Diaz, J. Vila-Comamala, O. Bunk, and A. Menzel, “Role of the illumination spatial-frequency spectrum for ptychography,” Phys. Rev. B **86**, 100103 (2012).
37. M. Odstrčil, M. Lebugle, M. Guizar-Sicairos, C. David, and M. Holler, “Towards optimized illumination for high-resolution ptychography,” Opt. Express **27**, 14981 (2019).

38. P. Helfenstein, I. Mohacsi, R. Rajeev, and Y. Ekinci, “Scanning coherent diffractive imaging methods for actinic extreme ultraviolet mask metrology,” J. Micro/Nanolithography, MEMS, MOEMS **15**, 034006 (2016).
39. T. F. Qahtan, M. A. Gondal, I. O. Alade, and M. A. Dastageer, “Fabrication of Water Jet Resistant and Thermally Stable Superhydrophobic Surfaces by Spray Coating of Candle Soot Dispersion,” Sci. Reports **7**, 7531 (2017).
40. O. Bunk, M. Dierolf, S. Kynde, I. Johnson, O. Marti, and F. Pfeiffer, “Influence of the overlap parameter on the convergence of the ptychographical iterative engine,” Ultramicroscopy **108**, 481–487 (2008).
41. X. Huang, H. Yan, R. Harder, Y. Hwu, I. K. Robinson, and Y. S. Chu, “Optimization of overlap uniformness for ptychography,” Opt. Express **22**, 12634 (2014).
42. K. Wakonig, H.-C. Stadler, M. Odstrčil, E. H. R. Tsai, A. Diaz, M. Holler, I. Usov, J. Raabe, A. Menzel, and M. Guizar-Sicairos, “PtychoShelves , a versatile high-level framework for high-performance analysis of ptychographic data,” J. Appl. Crystallogr. **53**, 574–586 (2020).
43. P. Thibault, M. Dierolf, O. Bunk, A. Menzel, and F. Pfeiffer, “Probe retrieval in ptychographic coherent diffractive imaging,” Ultramicroscopy **109**, 338–343 (2009).
44. M. Odstrčil, A. Menzel, and M. Guizar-Sicairos, “Iterative least-squares solver for generalized maximum-likelihood ptychography,” Opt. Express **26**, 3108 (2018).
45. P. Thibault and A. Menzel, “Reconstructing state mixtures from diffraction measurements,” Nature **494**, 68–71 (2013).
46. M. Odstrcil, P. Baksh, S. A. Boden, R. Card, J. E. Chad, J. G. Frey, and W. S. Brocklesby, “Ptychographic coherent diffractive imaging with orthogonal probe relaxation,” Opt. Express **24**, 8360 (2016).
47. D. L. Windt, “IMD—Software for modeling the optical properties of multilayer films,” Comput. Phys. **12**, 360 (1998).
48. M. Sánchez del Río and R. J. Dejus, “XOP v2.4: recent developments of the x-ray optics software toolkit,” in *Advances in Computational Methods for X-Ray Optics II,* vol. 8141 M. Sanchez del Rio and O. Chubar, eds. (SPIE, 2011), p. 814115.
49. B. Wang, N. Brooks, M. Tanksalvala, Y. Esashi, N. Jenkins, P. Johnsen, I. Binnie, G. Gui, Y. Shao, M. Murnane, and H. Kapteyn, “Robust and reliable actinic ptychographic imaging of highly periodic structures in EUV photomasks,” in *Photomask Technology 2022,* B. S. Kasprowicz and T. Liang, eds. (SPIE, 2022), December 2022, p. 50.
50. D. G. Lee, Y. W. Kim, S. Moon, and J. Ahn, “Effect of wrinkles on extreme ultraviolet pellicle reflectivity and local critical dimension,” Appl. Opt. **61**, 5965 (2022).

Declaration of interests

☒ The authors declare that they have no known competing financial interests or personal relationships that could have appeared to influence the work reported in this paper.

☐ The authors declare the following financial interests/personal relationships which may be considered as potential competing interests: